PHYSICAL REVIEW B **109**, L180507 (2024)

Letter

Superconducting, plastic, and superionic states driven by four-membered lithium rings in a high-pressure lithium-lead compound

Qing Lu,[1] Chi Ding,[1,*] Qiuhan Jia,[1] Shuning Pan,[1] Jiuyang Shi,[1] Yu Han,[1] Junjie Wang,[1] Xiaomeng Wang,[2] Dingyu Xing,[1] and Jian Sun[1,†]

[1]*National Laboratory of Solid State Microstructures, School of Physics, and Collaborative Innovation Center of Advanced Microstructures, Nanjing University, Nanjing 210093, China*

[2]*School of Physics and Electronic-Electrical Engineering, Ningxia University, Yinchuan 750021, China*

(Received 7 November 2023; revised 26 February 2024; accepted 22 April 2024; published 22 May 2024)

Using a combination of crystal structure search methods, first-principles calculations, and machine learning potential based simulations, we explored the lithium-lead system and predicted five phases: I_4/mcm $LiPb_2$, $Pnma$ LiPb, I_4/mmm Li_4Pb, $C2/m$ Li_5Pb, and $Cmcm$ Li_6Pb. Among them, I_4/mmm Li_4Pb displayed remarkable properties, including superconductivity, plasticity, and superionic behavior at varying temperature ranges. At lower temperatures, I_4/mmm Li_4Pb manifests superconductivity with a critical transition temperature of 4–5 K. Its superconducting behavior is attributed to the interplay between the B_{2g} vibration mode, which signifies the rotational motion of four-membered lithium rings within the stacking layer, and the participation of p-orbital electrons. As temperature rises, I_4/mmm Li_4Pb first transitions into a plastic phase, marked by continuous collective rotation of intralayer four-membered lithium rings, and then shows superionic behavior characterized by the emergence of interlayer lithium atom diffusion. These unique behaviors stem from stronger Li-Li bonds within four-membered lithium rings and a lower energy barrier for collective motion, distinct from interstitial localized electrons in electrides found in other lithium-based systems. This work provides an intriguing platform for exploring distinct states and establishes a correlation between various physical phenomena and the system's structure and bonding.

DOI: 10.1103/PhysRevB.109.L180507

Superconductivity, plasticity, and superionicity are typically associated with vastly different material states, often occurring under distinct temperature and pressure conditions. For instance, superconductivity usually arises at extremely low temperatures, facilitating the formation of the superconducting energy gap in metals [1]. In stark contrast, plastic and superionic phases tend to manifest at elevated temperatures. The plastic state is frequently observed in insulating molecular crystals, with molecules, like methane, exhibiting disordered rotational motion at higher temperatures [2]. Superionic behavior, on the other hand, can emerge across a spectrum of materials, ranging from molecular crystals to alloys [3–7]. Its significance extends to applications in planetary science and battery materials [8]. Remarkably, high pressure serves as an effective tool to induce these states individually. For example, superconductivity with a critical transition temperature (T_c) of 36 K was detected at 260 GPa in the case of scandium [9], and hydrogen sulfide (H_3S) exhibited T_c values of 191–204 K at 200 GPa [10]. While recent research in planetary science has shed light on the relevance of plasticity and superionicity, such as in He-NH_3 within icy giant planets [11,12], the integration of these three distinct material states and the exploration of their potential connections have remained limited due to the scarcity of suitable systems for study.

Recent investigations have uncovered intriguing phenomena of superconductivity and superionicity in various binary lithium compounds, including Li_5N [13], Li_7As [14], and Li_6Al [15]. The pivotal role of lithium in these behaviors cannot be understated: lithium, as a simple metal, exhibits eminent superconductivity above 20 GPa [16]. Its lightweight nature facilitates diffusion and also makes it especially relevant in applications such as lithium-based batteries [17]. Notably, these compounds share a common characteristic—they are electrides housing interstitial anionic electrons (IAEs) [18–23]. While the influence of IAEs on superconductivity remains a topic of debate [24–26], their substantial impact on dynamic behaviors, including collective motion, is recognized [27,28]. A recent study [29] has shed light on the superionic behavior of hydrogen in nonelectride superconductor LaH_{10} [30], suggesting that the emergence of superionicity and superconductivity in superhydrides does not rely on IAEs. However, given the heavier nature of lithium compared to hydrogen, the necessity of electride properties for these phenomena in binary lithium alloys remains an open question. Furthermore, while lithium atoms in Li_7As have been reported to exhibit both plastic and superionic behavior at 1000 K [14], the specific transition between these states in binary lithium alloys remains an unexplored avenue of research.

In this Letter, we present the results of our comprehensive investigation into the lithium-lead system. This system holds significant importance due to its widespread utilization as coolants and tritium breeders in nuclear fusion reactors [31]. Using our self-developed structure searching package MAGUS

---

[*] chiding@nju.edu.cn

[†] jiansun@nju.edu.cn

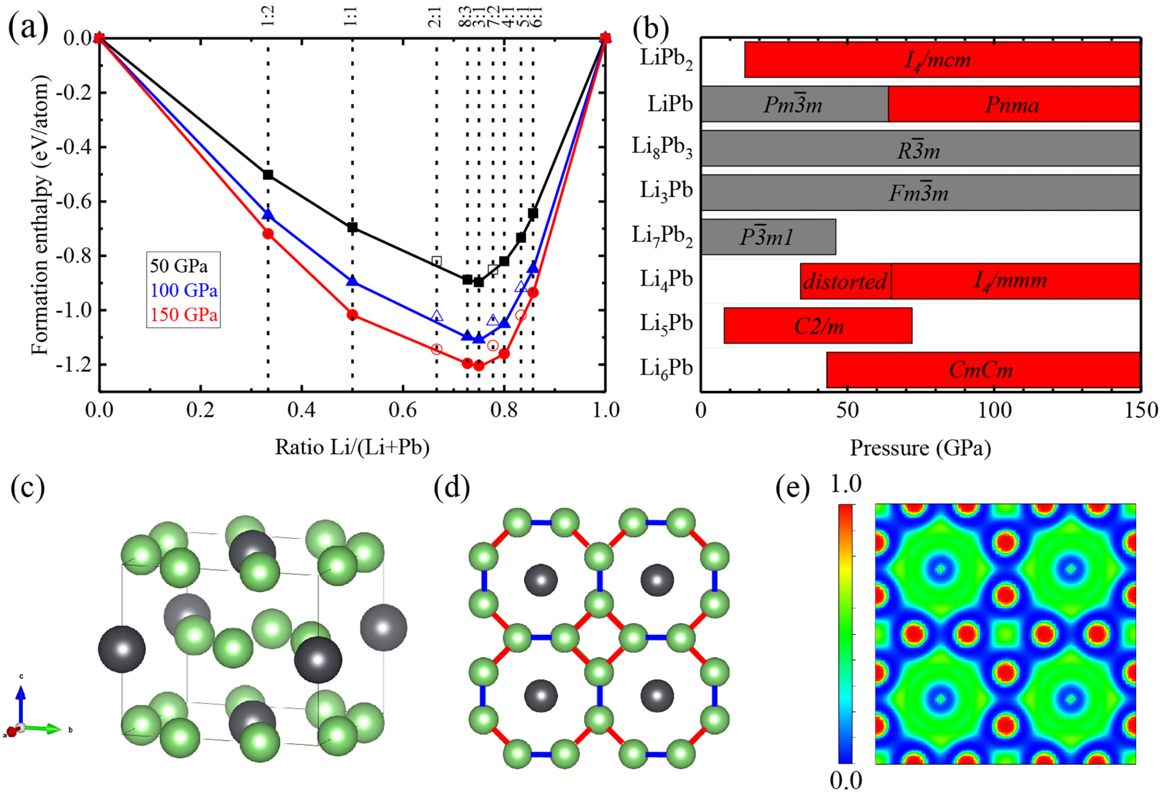

FIG. 1. Thermodynamic stability and crystal structure of lithium-lead system. (a) Convex hulls at 50, 100, and 150 GPa. Solid symbols represent thermodynamically stable structures, while hollow symbols denote unstable ones. (b) Phase diagrams from 0 to 150 GPa. The structures predicted in this work are indicated in red, while previously known ones are shown in gray bars. (c) The crystal structure of I_4/mmm Li_4Pb. (d) T-graphene-like stacking layer, and (e) electron localization function (ELF) map for the stacking layer (001) of I_4/mmm Li_4Pb at 50 GPa. For intuitive understanding, we added Li-Li bonds inside (red) and outside (blue) rings in the stacking layer in (d). Lithium and lead atoms are depicted as green and black balls, respectively.

(machine learning and graph theory assisted universal structure searcher) [32–34], we have elucidated a comprehensive phase diagram of the lithium-lead system spanning pressures from 50 to 150 GPa, revealing the presence of several phases. Among these, the I_4/mmm Li_4Pb phase demonstrates diverse electronic and dynamic properties at different temperatures, including superconductivity, plasticity, and superionic behavior with the help of four-membered lithium rings instead of IAEs. This work underscores the pivotal role of structure in shaping material properties and behaviors.

In Figs. 1(a) and 1(b), we illustrate the convex hulls and phase diagrams of the lithium-lead system. Notably, the previously known $Pm\bar{3}m$ LiPb undergoes a phase transition at approximately 64 GPa, transforming into a predicted $Pnma$ phase, a behavior commonly observed in various systems [35,36]. The $P\bar{3}m1$ Li_7Pb_2 is thermodynamically stable only below 46 GPa, while the $R\bar{3}m$ Li_8Pb_3 and $Fm\bar{3}m$ Li_3Pb remain stable up to at least 150 GPa. Additionally, our predictions unveil several structures that stabilize within specific pressure ranges. For instance, $C2/m$ Li_5Pb remains stable at lower pressures, ranging from 8 to 72 GPa, whereas I_4/mcm $LiPb_2$, I_4/mmm Li_4Pb, and $Cmcm$ Li_6Pb maintain their stability at higher pressures, extending to at least 150 GPa. Intriguingly, we observed that I_4/mmm Li_4Pb becomes metastable, transforming into a distorted structure below 65 GPa, as analyzed in subsequent dynamic properties assessments. Such a wide stable region suggests the likelihood of synthesizing these predicted structures, establishing a robust platform for exploring various physical properties. All predicted structures are visually represented in Fig. 1 and Fig. S2 in the Supplemental Material (SM) [37] (see also Refs. [38–48] therein), with detailed lattice constants and atomic Wyckoff positions listed in Table SI [37]. Notably, Li_4Pb, Li_5Pb, and Li_6Pb adopt layeredlike structures, where Pb atoms occupy the central positions within Li atom polygons. (Despite the planar stacking behavior, the systems are still bulk materials with comparable in-plane and out of plane Li-Pb bond strength.) For instance, in Li_4Pb, the combination of octagonal and quadrangular Li atom networks forms a planar structure reminiscent of T-graphene [49], with Pb atoms situated at the center of Li octagons [see Figs. 1(c) and 1(d)]. Similarly, Pb atoms in Li_5Pb and Li_6Pb occupy central positions within Li octagons and heptagons, respectively. Remarkably, these structures exhibit distinctive electronic behaviors. For instance, based on the electron localization function (ELF), both Li_5Pb and Li_6Pb are classified as electrides (Fig. S4 [37]), whereas Li_4Pb lacks IAEs [Fig. 1(e)], owing to its unique stacking arrangement of planar structures. In Li_6Pb, Li atom pentagons within the same stacking layer are adjacent to either Pb atoms or Li atoms. However, only the latter can host localized electrons, owing to the cavities enclosed by Li atoms and the electronegativity difference between Li and Pb [50]. Additionally, an open

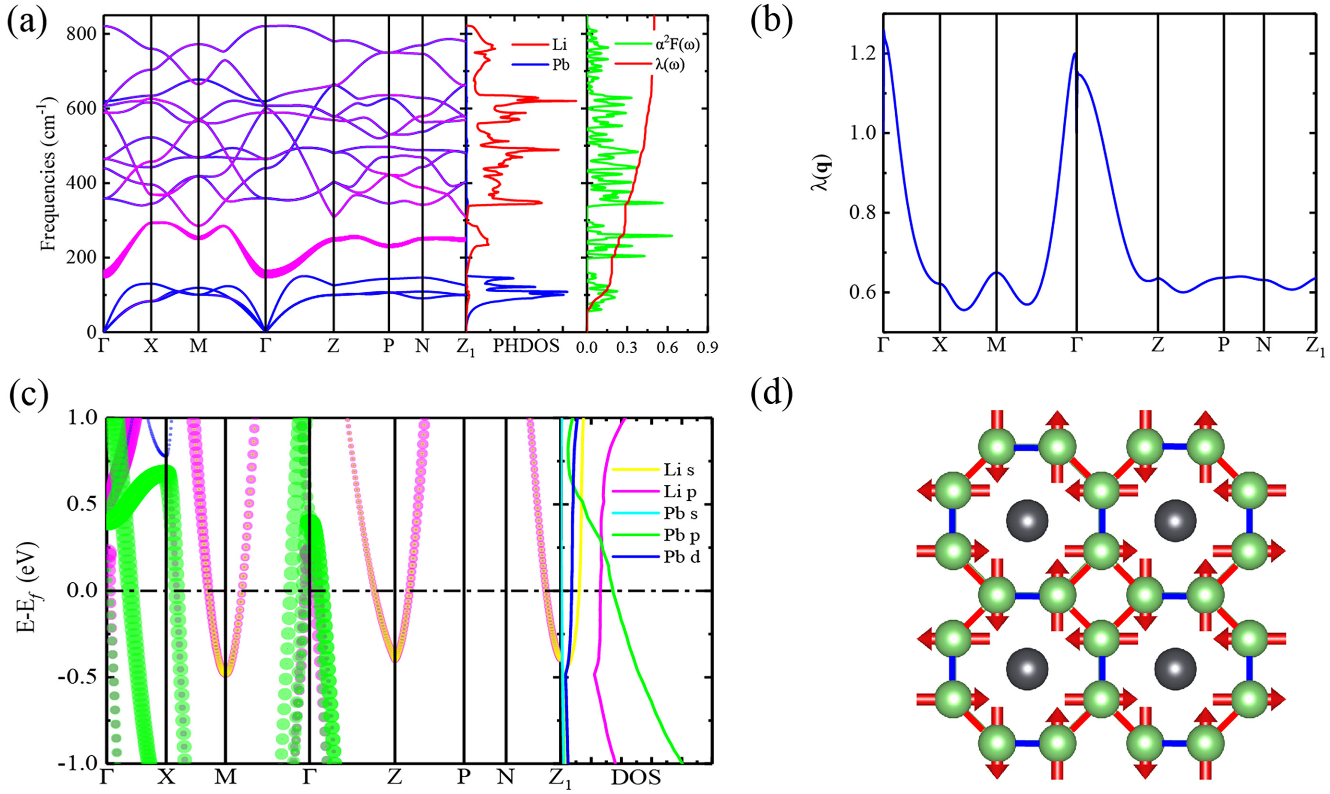

FIG. 2. Superconducting properties of I_4/mmm Li_4Pb at 50 GPa. (a) The phonon spectrum, PHDOS, $\alpha^2F(\omega)$, and $\lambda(\omega)$. The magenta circle sizes are proportional to the coupling strength. (b) Accumulated $\boldsymbol{q}$-dependent coupling factor $\lambda(\boldsymbol{q})$ along the Brillouin zone path, which follows the equation $\lambda(\boldsymbol{q}) = \sum_j \frac{\gamma_{qj}}{\omega_{qj}^2}$ and is normalized by $\lambda(\Gamma)$. (c) Orbital-projected band structure and density of states. The size of the colored circles corresponds to the contribution of electrons from the respective orbital, as indicated in the labels. (d) B_{2g} mode at the Γ point, as depicted with red arrows.

channel formed by the one-dimensional arrangement of parallelepipeds in Li_5Pb leads to the delocalization of interstitial electrons along the stacking direction. Conversely, in Li_4Pb, the quadrilateral formed by Li atoms is adjacent to Pb atoms along the stacking direction, resulting in the absence of IAEs below 150 GPa.

Our investigation further extended to the superconducting properties of I_4/mmm Li_4Pb as illustrated in Fig. 2 and Fig. S8 [37]. Notably, the phonon branches exhibit a distinct division into two regions. The low-frequency zone is predominantly characterized by the vibrations of Pb atoms, while the high-frequency zone is dominated by the vibrations of Li atoms, primarily due to the substantial difference in atom masses. This division in vibrations results in an energy gap observed in the phonon density of states (PHDOS), reaching 200 cm^{-1} at 150 GPa, a consequence of phonon hardening in the optical branches attributed to the reduction in Li-Li bond length. This substantial gap has a significant impact on the electron-phonon coupling strength λ. When compared to other binary lithium systems [13–15,51–54], Li_4Pb exhibits a relatively lower value of T_c, primarily attributed to the decoupling of acoustic and optical branches and the inversion relationship between frequency and accumulated $\lambda(\omega)$. With increasing pressure, λ remains relatively stable, hovering around 0.5, while $\omega_{\log}$, representing the characteristic phonon frequency, increases from 325.9 to 418.7 K due to optical phonon hardening, subsequently elevating T_c from 4.0 to 4.9 K. Figure 2(a) also indicates that the most substantial coupling strength predominantly stems from the lowest optical branch. Furthermore, Fig. 2(b) demonstrates that along our calculated Brillouin path, the coupling strength reaches its global maximum around the Γ point and achieves local maxima at various other high-symmetry points, such as the *M* and *Z* points.

To delve into the electron-phonon coupling, we analyzed the vibration mode of the lowest optical branch at the Γ point and the orbital-projected band structure. Figure 2(d) highlights the B_{2g} mode, representing the in-plane rotation of four-membered lithium rings in the stacking layer. The corresponding projected band structure in Fig. 2(c) indicates that the dominant contribution near the Fermi level stems from the *p* orbitals of Li and Pb atoms. Therefore, the primary source of λ arises from the coupling between the in-plane B_{2g} vibration mode and *p*-orbital electrons. We also assessed the superconducting properties of various lithium-lead compounds under different pressures, as summarized in Table SII [37]. Predictably, their T_c values remain quite low due to the substantial decoupling observed between the acoustic and optical branches, as previously discussed and illustrated in Fig. S6 [37].

The high-temperature behavior of I_4/mmm Li_4Pb was also subjected to detailed analysis. At 50 GPa, I_4/mmm Li_4Pb retains its dynamic stability until it reaches 400 K, at which point lithium atoms deviate from their equilibrium positions

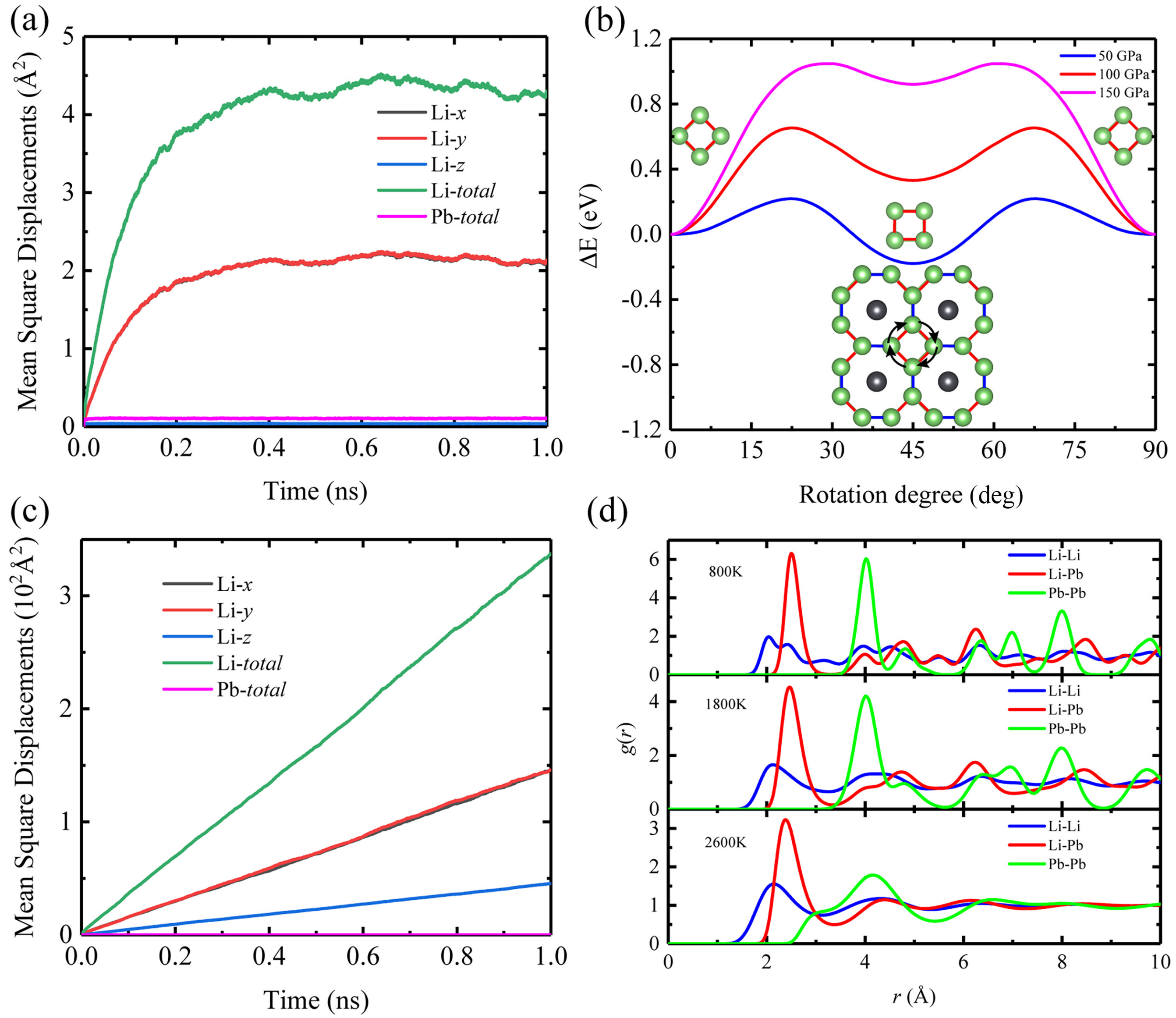

FIG. 3. Dynamic properties of I_4/mmm Li_4Pb around 50 GPa. MSDs of Li and Pb atoms at (a) 800 K (plastic state) and (c) 1800 K (superionic state). (b) Rotation energy barrier of a single four-membered lithium ring in a 3 × 3 × 3 supercell. The pattern of collective rotation of four-membered lithium rings is visualized with black arrows. (d) Radial distribution function $g(r)$ between Li-Li, Li-Pb, and Pb-Pb at different temperatures.

while lead atoms continue to vibrate around their equilibrium positions. Trajectories presented in the SM [37] reveal that the displacement of lithium atoms occurs within the stacking layer, involving a 45° rotation of four-membered lithium rings around the center of the cavities. Eventually, the system transitions into a distorted solid phase once it reaches dynamic equilibrium. To scrutinize the energy differences during this distortion process, we employed the nudged elastic band (NEB) method [55], as depicted in Fig. 3(b). The calculated energy minimum path corroborates the rotation of four-membered lithium rings, aligning with the results from machine-learning molecular dynamics (MLMD). The details of the validity of our MLMD calculations is presented in the SM [37]. Furthermore, our NEB analysis discloses that the distorted structure at 50 GPa possesses lower energy compared to the undistorted one. This suggests that within practical materials containing multiple four-membered lithium rings under specific pressure conditions, I_4/mmm Li_4Pb exhibits metastability. At 400 K, the four-membered lithium rings surmount an energy barrier of 0.22 eV, corresponding to a rotation angle of 18°, and ultimately reach the global minimum of potential energy at 45°, resulting in the distorted solid phase. (Note that due to lattice distortion of local configurations and dynamic thermal fluctuations, a minority of rings continue to transition between these two states, as depicted in SM movies [37].)

As the temperature escalates to 800 K, the kinetic energy of the four-membered lithium rings becomes sufficiently substantial to surmount an energy barrier of 0.40 eV. Consequently, the rings begin to rotate freely within the stacking

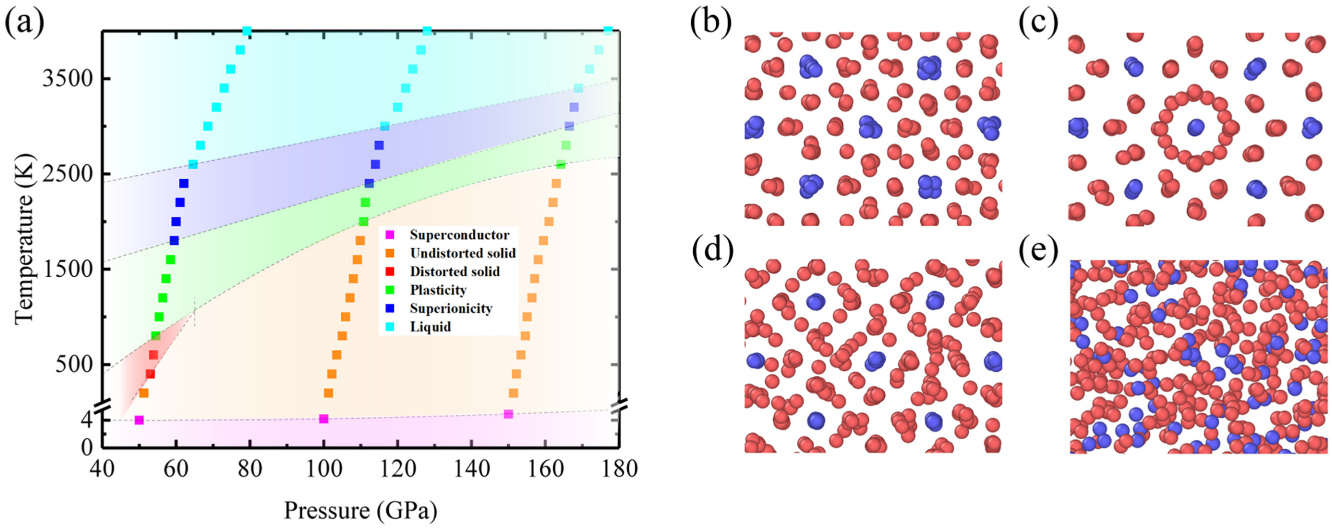

FIG. 4. Temperature induced behaviors of $I4/mmm$ Li_4Pb. Left: (a) Pressure-temperature phase diagram. The magenta, orange, red, green, blue, and cyan points (areas) represent superconductor, undistorted solid, distorted solid, plastic, superionic, and liquid phases, respectively. Right: Snapshots of different phases including (b) distorted solid, (c) plastic, (d) superionic, and (e) liquid states.

layer, signifying a transition to the plastic phase. The ideal mean square displacement (MSD) of lithium atoms over an infinite time can be computed using $\langle (r - r_0)^2 \rangle = \frac{2r_c^2}{2\pi}\int_0^{2\pi}(1-\cos\theta)d\theta = 2r_c^2$, where r_c corresponds to the rotation radius. The final saturated MSD value obtained is approximately 4.21 Å^2, consistent with our MLMD calculation presented in Fig. 3(a). Notably, plasticity is a phenomenon typically observed in molecular crystals. The emergence of the plastic state in Li_4Pb is attributed to its stacking layer, as ring diffusion frequently involves four atoms in several metals, owing to a lower migration barrier compared to the direct exchange of two atoms [56–58], a characteristic validated by our NEB calculations. Additionally, the absence of interstitial anionic electrons (IAEs) suggests a distinct mechanism compared to recently reported collective motion in Li_6Al [15] and chain melting in simple cubic Ca [27]. A noteworthy example highlighting the significance of the stacking layer is Li_3N, where lithium atoms within stacking layers commence migration around nitrogen atoms at 900 K [59,60].

As the temperature escalates to 1800 K, lithium atoms within the four-membered rings spanning different stacking layers surmount the interlayer energy barrier and commence vertical exchange, signifying a superionic behavior characterized by the simultaneous presence of intralayer and interlayer diffusion, as illustrated in Fig. 3(c). Furthermore, the substantial disparity observed between intralayer MSD and interlayer MSD points to a distinct diffusion mechanism in contrast to the random-walk diffusion characteristic of the liquid state. Upon reaching 2600 K, the lead lattice ultimately collapses, resulting in the system exhibiting liquidlike behavior.

Phase transitions are also discernible through the radial distribution function (RDF) $g(r)$, as depicted in Fig. 3(d) and Fig. S12 [37]. In Fig. 3(d), the transition from the solid state to the plastic state introduces orientation disorder and disrupts the long-range order of the lithium lattice. Consequently, the $g(r)$ of Li-Li at 800 K converges to 1. At 1800 K, lithium atoms initiate vertical diffusion, resulting in a smoother $g(r)$ of Li-Li. However, it still distinguishes itself from the liquid state, where the entire lattice maintains only short-range order and $g(r)$ rapidly converges to 1 with increasing distance. Trajectory movies and related snapshots are obtained in the SM [37] and Figs. 4(b)–4(e).

A comprehensive pressure-temperature phase diagram for $I4/mmm$ Li_4Pb is presented in Fig. 4. As pressure increases, the transition temperature from the solid phase rises rapidly, primarily attributed to the phonon hardening of lithium vibration modes, similar to the disappearance of the distorted solid phase. At 50 GPa, the lowest optical mode registers around 200 cm^{-1} with a growth rate of 100 cm^{-1} per 50 GPa, rendering it less susceptible to softening at elevated temperatures. From an electronic properties perspective, as shown in the projected crystal orbital Hamilton population [61] (pCOHP) calculations depicted in Fig. S10 [37], the strength of Li-Li bonds within four-membered lithium rings is considerably higher and exhibits a swifter growth rate under increased pressure compared to other bonds, facilitating the detection of collective motions in both plastic and superionic states.

In summary, our investigation on the lithium-lead system, combining first-principles and machine learning potential based calculations, has unveiled a diverse and intricate phase diagram. We have identified several thermodynamically stable bulk phases, including Li_4Pb, Li_5Pb, and Li_6Pb, all characterized by a homogeneous planar stacking structure. Notably, the arrangement of stacking layers plays a pivotal role in the formation of IAEs, distinguishing Li_4Pb as a nonelectride, and setting it apart from the other two structures. $I4/mmm$ Li_4Pb exhibits remarkable properties, including superconductivity, plasticity, and superionicity, which are intricately linked to the varying strengths of Li-Li bonds and lower migration barriers within the four-membered lithium rings in Li_4Pb's stacking layer, all achieved without the involvement of IAEs. These phenomena fall within experimentally feasible pressure ranges and promise to enhance our understanding of the behavior of lithium-based alloys across different temperature regimes.

J.S. gratefully acknowledges the financial support from the National Key R&D Program of China (Grant No. 2022YFA1403201), the National Natural Science Foundation of China (Grants No. 12125404 and No. 11974162), and the Fundamental Research Funds for the Central Universities. The calculations were carried out using supercomputers at the High Performance Computing Center of the Collaborative Innovation Center of Advanced Microstructures, the high-performance supercomputing center of Nanjing University.

[1] P. B. Allen and R. C. Dynes, Transition temperature of strong-coupled superconductors reanalyzed, Phys. Rev. B **12**, 905 (1975).

[2] J. Timmermans, Plastic crystals: A historical review, J. Phys. Chem. Solids **18**, 1 (1961).

[3] M. Millot, F. Coppari, J. R. Rygg, A. Correa Barrios, S. Hamel, D. C. Swift, and J. H. Eggert, Nanosecond x-ray diffraction of shock-compressed superionic water ice, Nature (London) **569**, 251 (2019).

[4] B. Cheng, M. Bethkenhagen, C. J. Pickard, and S. Hamel, Phase behaviours of superionic water at planetary conditions, Nat. Phys. **17**, 1228 (2021).

[5] H.-F. Li, A. R. Oganov, H. Cui, X.-F. Zhou, X. Dong, and H.-T. Wang, Ultrahigh-pressure magnesium hydrosilicates as reservoirs of water in early earth, Phys. Rev. Lett. **128**, 035703 (2022).

[6] Y. He, S. Sun, D. Y. Kim, B. G. Jang, H. Li, and H. Mao, Superionic iron alloys and their seismic velocities in earth's inner core, Nature (London) **602**, 258 (2022).

[7] C. Liu, H. Gao, Y. Wang, R. J. Needs, C. J. Pickard, J. Sun, H.-T. Wang, and D. Xing, Multiple superionic states in helium–water compounds, Nat. Phys. **15**, 1065 (2019).

[8] Q. Hu and H. Mao, Role of hydrogen and proton transportation in earth's deep mantle, Matter Radiat. Extremes **6**, 68101 (2021).

[9] J. Ying, S. Liu, Q. Lu, X. Wen, Z. Gui, Y. Zhang, X. Wang, J. Sun, and X. Chen, Record high 36 K transition temperature to the superconducting state of elemental scandium at a pressure of 260 GPa, Phys. Rev. Lett. **130**, 256002 (2023).

[10] D. Duan, Y. Liu, F. Tian, D. Li, X. Huang, Z. Zhao, H. Yu, B. Liu, W. Tian, and T. Cui, Pressure-induced metallization of dense $(H_2S)_2H_2$ with high-T_c superconductivity, Sci. Rep. **4**, 6968 (2014).

[11] C. Liu, H. Gao, A. Hermann, Y. Wang, M. Miao, C. J. Pickard, R. J. Needs, H.-T. Wang, D. Xing, and J. Sun, Plastic and superionic helium ammonia compounds under high pressure and high temperature, Phys. Rev. X **10**, 021007 (2020).

[12] J. Shi, W. Cui, J. Hao, M. Xu, X. Wang, and Y. Li, Formation of ammonia–helium compounds at high pressure, Nat. Commun. **11**, 3164 (2020).

[13] Z. Wan, C. Zhang, T. Yang, W. Xu, and R. Zhang, Predicted superconductivity and superionic state in the electride Li_5N under high pressure, New J. Phys. **24**, 113012 (2022).

[14] Z. Wan, W. Xu, T. Yang, and R. Zhang, As-Li electrides under high pressure: Superconductivity, plastic, and superionic states, Phys. Rev. B **106**, L060506 (2022).

[15] X. Wang, Y. Wang, J. Wang, S. Pan, Q. Lu, H. T. Wang, D. Xing, and J. Sun, Pressure stabilized lithium-aluminum compounds with both superconducting and superionic behaviors, Phys. Rev. Lett. **129**, 246403 (2022).

[16] K. Shimizu, H. Ishikawa, D. Takao, T. Yagi, and K. Amaya, Superconductivity in compressed lithium at 20 K, Nature (London) **419**, 597 (2002).

[17] J.-M. Tarascon and M. Armand, Issues and challenges facing rechargeable lithium batteries, Nature (London) **414**, 359 (2001).

[18] B. Rousseau and N. W. Ashcroft, Interstitial electronic localization, Phys. Rev. Lett. **101**, 046407 (2008).

[19] X. Dong *et al.*, A stable compound of helium and sodium at high pressure, Nat. Chem. **9**, 440 (2017).

[20] T. Huang, C. Liu, J. Wang, S. Pan, Y. Han, C. J. Pickard, R. Helled, H.-T. Wang, D. Xing, and J. Sun, Metallic aluminum suboxides with ultrahigh electrical conductivity at high pressure, Research **2022**, 9798758 (2022).

[21] M. S. Miao and R. Hoffmann, High pressure electrides: A predictive chemical and physical theory, Acc. Chem. Res. **47**, 1311 (2014).

[22] C. Liu, S. A. Nikolaev, W. Ren, and L. A. Burton, Electrides: A review, J. Mater. Chem. C **8**, 10551 (2020).

[23] J. Feng, R. G. Hennig, N. W. Ashcroft, and R. Hoffmann, Emergent reduction of electronic state dimensionality in dense ordered Li-Be alloys, Nature (London) **451**, 445 (2008).

[24] Z. Liu, Q. Zhuang, F. Tian, D. Duan, H. Song, Z. Zhang, F. Li, H. Li, D. Li, and T. Cui, Proposed superconducting electride Li_6C by *sp*-hybridized cage states at moderate pressures, Phys. Rev. Lett. **127**, 157002 (2021).

[25] Z. Zhao, S. Zhang, T. Yu, H. Xu, A. Bergara, and G. Yang, Predicted pressure-induced superconducting transition in electride Li_6P, Phys. Rev. Lett. **122**, 097002 (2019).

[26] Z. Liu, D. Duan, Q. Zhuang, and T. Cui, High-temperature superconductivity in electrides dominated by hybridized *p*-orbital-like electride states, Phys. Rev. B **108**, L100507 (2023).

[27] Y. Wang, J. Wang, A. Hermann, C. Liu, H. Gao, E. Tosatti, H. T. Wang, D. Xing, and J. Sun, Electronically driven 1D cooperative diffusion in a simple cubic crystal, Phys. Rev. X **11**, 011006 (2021).

[28] H. Zong, V. N. Robinson, A. Hermann, L. Zhao, S. Scandolo, X. Ding, and G. J. Ackland, Free electron to electride transition in dense liquid potassium, Nat. Phys. **17**, 955 (2021).

[29] H. Wang, P. T. Salzbrenner, I. Errea, F. Peng, Z. Lu, H. Liu, L. Zhu, C. J. Pickard, and Y. Yao, Quantum structural fluxion in superconducting lanthanum polyhydride, Nat. Commun. **14**, 1674 (2023).

[30] A. P. Drozdov *et al.*, Superconductivity at 250 K in lanthanum hydride under high pressures, Nature (London) **569**, 528 (2019).

[31] E. Mas de les Valls, L. A. Sedano, L. Batet, I. Ricapito, A. Aiello, O. Gastaldi, and F. Gabriel, Lead–lithium eutectic

material database for nuclear fusion technology, J. Nucl. Mater. **376**, 353 (2008).

[32] J. Wang, H. Gao, Y. Han, C. Ding, S. Pan, Y. Wang, Q. Jia, H.-T. Wang, D. Xing, and J. Sun, MAGUS: Machine learning and graph theory assisted universal structure searcher, Natl. Sci. Rev. **10**, nwad128 (2023).

[33] K. Xia, H. Gao, C. Liu, J. Yuan, J. Sun, H.-T. Wang, and D. Xing, A novel superhard tungsten nitride predicted by machine-learning accelerated crystal structure search, Sci. Bull. **63**, 817 (2018).

[34] H. Gao, J. Wang, Y. Han, and J. Sun, Enhancing crystal structure prediction by decomposition and evolution schemes based on graph theory, Fundam. Res. **1**, 466 (2021).

[35] D. Errandonea *et al.*, Experimental and theoretical confirmation of an orthorhombic phase transition in niobium at high pressure and temperature, Commun. Mater. **1**, 60 (2020).

[36] S. Pal, R. Arora, S. Roychowdhury, L. Harnagea, K. Saurabh, S. Shenoy, D. V. S. Muthu, K. Biswas, U. V. Waghmare, and A. K. Sood, Pressure-induced phase transitions in the topological crystalline insulator SnTe and its comparison with semiconducting SnSe: Raman and first-principles studies, Phys. Rev. B **101**, 155202 (2020).

[37] See Supplemental Material at http://link.aps.org/supplemental/10.1103/PhysRevB.109.L180507 for more details about calculation methods, lattice constants, electronic properties, superconducting properties, and dynamic properties.

[38] G. Kresse and J. Furthmüller, Efficiency of *ab-initio* total energy calculations for metals and semiconductors using a plane-wave basis set, Comput. Mater. Sci. **6**, 15 (1996).

[39] J. P. Perdew, K. Burke, and M. Ernzerhof, Generalized gradient approximation made simple, Phys. Rev. Lett. **77**, 3865 (1996).

[40] A. Stukowski, Visualization and analysis of atomistic simulation data with OVITO—the open visualization tool, Model. Simul. Mater. Sci. Eng. **18**, 015012 (2010).

[41] P. E. Blöchl, Projector augmented-wave method, Phys. Rev. B **50**, 17953 (1994).

[42] A. Togo and I. Tanaka, First principles phonon calculations in materials science, Scr. Mater. **108**, 1 (2015).

[43] A. Togo, First-principles phonon calculations with PHONOPY and PHONO3PY, J. Phys. Soc. Jpn. **92**, 12001 (2022).

[44] W. G. Hoover, Canonical dynamics: Equilibrium phase-space distributions, Phys. Rev. A **31**, 1695 (1985).

[45] A. P. Thompson *et al.*, LAMMPS—a flexible simulation tool for particle-based materials modeling at the atomic, meso, and continuum scales, Comput. Phys. Commun. **271**, 108171 (2022).

[46] I. S. Novikov, K. Gubaev, E. V. Podryabinkin, and A. V. Shapeev, The MLIP package: Moment tensor potentials with MPI and active learning, Mach. Learn. Sci. Technol. **2**, 025002 (2021).

[47] P. Giannozzi *et al.*, QUANTUM ESPRESSO: A modular and open-source software project for quantum simulations of materials, J. Phys.: Condens. Matter **21**, 395502 (2009).

[48] P. B. Allen, Neutron spectroscopy of superconductors, Phys. Rev. B **6**, 2577 (1972).

[49] Q. Gu, D. Xing, and J. Sun, Superconducting single-layer *T*-graphene and novel synthesis routes, Chin. Phys. Lett. **36**, 097401 (2019).

[50] X. Dong, A. R. Oganov, H. Cui, X.-F. Zhou, and H.-T. Wang, Electronegativity and chemical hardness of elements under pressure, Proc. Natl. Acad. Sci. USA **119**, e2117416119 (2022).

[51] Y. Xu, C. Chen, S. Wang, and X. Sun, Novel structures and superconductivities of calcium-lithium alloys at high pressures: A first-principles study, J. Alloys Compd. **669**, 101 (2016).

[52] Y. Xu, C. Chen, and B. Wu, Superconductivity in ordered LiBe alloy under high pressure: A first-principles study, Solid State Commun. **152**, 151 (2012).

[53] X. Zhang and A. Zunger, Altered reactivity and the emergence of ionic metal ordered structures in Li-Cs at high pressures, Phys. Rev. Lett. **104**, 245501 (2010).

[54] Y. Xie, A. R. Oganov, and Y. Ma, Novel high pressure structures and superconductivity of $CaLi_2$, Phys. Rev. Lett. **104**, 177005 (2010).

[55] D. Sheppard, P. Xiao, W. Chemelewski, D. D. Johnson, and G. Henkelman, A generalized solid-state nudged elastic band method, J. Chem. Phys. **136**, 74103 (2012).

[56] L. P. Yu, X. H. Zhou, L. Lu, X. L. Wu, and F. J. Wang, Recent developments of nanomaterials and nanostructures for high-rate lithium ion batteries, ChemSusChem **13**, 5361 (2020).

[57] C. Zener, Ring diffusion in metals, Acta Crystallogr. **3**, 346 (1950).

[58] X. He, Y. Zhu, and Y. Mo, Origin of fast ion diffusion in superionic conductors, Nat. Commun. **8**, 15893 (2017).

[59] S. Ihara and K. Suzuki, Molecular dynamics study of Li_3N, J. Phys. Soc. Jpn. **54**, 2607 (1985).

[60] M. L. Wolf, Observation of solitary-wave conduction in a molecular dynamics simulation of the superionic conductor Li_3N, J. Phys. C: Solid State Phys. **17**, L285 (1984).

[61] V. L. Deringer, A. L. Tchougréeff, and R. Dronskowski, Crystal orbital Hamilton population (COHP) analysis as projected from plane-wave basis sets, J. Phys. Chem. A **115**, 5461 (2011).